Understanding Post-main-sequence Stellar Magnetism: On the Origin of Pollux's Weak Surface Magnetic Field

Louis Amard, Allan Sacha Brun, Ana Palacios

The Astrophysical Journal, 974:311 (16pp), 2024 October 20 https://doi.org/10.3847/1538-4357/ad6cd0

Understanding Post-main-sequence Stellar Magnetism: On the Origin of Pollux's Weak Surface Magnetic Field

Louis Amard[1], Allan Sacha Brun[1], and Ana Palacios[2]
[1] Département d'Astrophysique/AIM, CEA/IRFU, CNRS/INSU, Univ. Paris-Saclay & Univ. de Paris F-91191 Gif-sur-Yvette, France; louis.amard@cea.fr
[2] LUPM, Université de Montpellier, Place Eugène Bataillon, 34095 Montpellier, France
Received 2024 April 26; revised 2024 July 12; accepted 2024 August 6; published 2024 October 18

Abstract

The magnetic field of red giants is still poorly understood today. Close to the core, asteroseismology has revealed magnetic fields of several hundred thousand gauss, but close to the surface, spectropolarimetric observations of the red giant Pollux only showed an average field of the order of 1 G. Using the ASH code, we conduct a series of 3D nonlinear magnetohydrodynamical simulations aiming at modeling the dynamo process operating within the extended convective envelope of a star similar to the red giant Pollux. We find that the dynamo is efficient even for the slow rotation considered and that large-scale fields are generated and maintained. We further test the correlation between the scale of the convective motions and the surface magnetic field geometry by varying the Prandtl number in our simulations. We show in particular that the value and the geometry of the modeled surface field depend directly on the coupling scales between the magnetic and the velocity fields, with larger convective cells leading to a stronger large-scale magnetic field. We also verify that the dynamo and the geometry of the resulting field are robust against a change of the initial conditions. We then compare our simulations to the observed field and find average $|B_\ell|$ of about 7 G for the simulation with large convective cells, and down to 2 G for the smaller-scale simulation, very close to the observed value. Finally, we suggest the possibility of the reversal of the red giant's magnetic field.

Unified Astronomy Thesaurus concepts: Stellar convection envelopes (299); Magnetohydrodynamical simulations (1966); Late-type giant stars (908); Stellar magnetic fields (1610)

1. Introduction

Single red giant stars are expected to have weak surface magnetic fields, if any, due to their large radius and slow surface rotation. First evidenced by activity indicators (H. Korhonen 2014), surface magnetic fields have been measured via Zeeman signatures using spectropolarimetry in a significant sample of about 50 red giants of G and K types with different rotation rates gathered by M. Aurière et al. (2015; see also R. Konstantinova-Antova et al. 2024). For the active stars of this sample with rotation periods between 25 and 200 days, corresponding to giants known for their activity evidenced in the Ca II H&K lines or by large X-ray luminosities, the maximal longitudinal magnetic field and the rotation period are anticorrelated, the faster spinning stars having a larger maximum magnetic field. This correlation, also holding when comparing $\|B_{l,\max}\|$ and the Rossby number, is interpreted as evidence for an $\alpha-\omega$ dynamo operating in these stars. From an evolutionary point of view, the magnetic red giants appear to be intermediate-mass stars that populate two magnetic instability strips in the Hertzsprung–Russell (H-R) diagram: one centered on the red clump and the base of the red giant branch (RGB), and the other centered on the early asymptotic giant branch (AGB) phase (M. Aurière et al. 2015; C. Charbonnel et al. 2017). In these regions, the Rossby number, *Ro*,[3] drops below unity and the $\alpha-\Omega$ dynamo is expected to become stronger.

Associated with the question of the origin of the surface magnetic fields in red giants is that of their magnetism in general. Magnetic fields are expected to affect the frequencies of the oscillation modes by shifting them (D. O. Gough 1990), and in the past years, several studies have focused on the expected signatures of internal magnetic fields on the mixed-mode frequencies in red giant stars (P. Gomes & I. Lopes 2020; S. T. Loi 2021; S. Mathis & L. Bugnet 2023). Even more recently, magnetic fields were actually detected in the core of several tens of red giants using asteroseismology (G. Li et al. 2022, 2023; S. Deheuvels et al. 2023), opening a new window for the study of the magnetism of evolved stars. In the red giants with detected internal magnetic field, however, it is expected to be a fossil field with no ongoing generation process, and somewhat decorrelated from the surface magnetic field that is thought to be recent and resulting from a dynamo process acting within the convective envelope.

To probe the possible role of a dynamo in red giants, we have decided to focus on the giant Pollux (β *Geminorum*). Pollux is a very well studied close-by K0III-type single red giant (D. F. Gray 2014), bearing indications of weak magnetic activity in its Ca II H&K emission lines (K. G. Strassmeier et al. 1990), and exhibiting a sub-gauss level mean surface magnetic field discovered through spectropolarimetric observational campaigns (M. Aurière et al. 2009). Pollux was the first star discovered in the class of weakly magnetic G–K giants (M. Aurière et al. 2015). Pollux also presents a very stable modulation of its radial velocity with a period of about 590 days, which is attributed to the presence of a planet orbiting this giant star (A. P. Hatzes & W. D. Cochran 1993; A. P. Hatzes et al. 2006). Coincidentally, the rotation period of Pollux extracted through Zeeman Doppler imaging (ZDI) from the mean longitudinal magnetic field signal B_ℓ is the longest of the rotation periods of giants measured so far, $P_{\rm rot} = 660 \pm 15$ days, and close to that of the radial velocity

[3] The Rossby number *Ro* is defined as the ratio of the surface rotation period $P_{\rm rot}$ to the convective turnover timescale $\tau_{\max}$ or $\tau_{Hp/2}$, depending on where this value is estimated within the convective envelope.

signal (M. Aurière et al. 2014, 2021). Finally, stellar pulsations have been uncovered in Pollux that are attributed to high-overtone radial pulsations (A. P. Hatzes et al. 2012), which allowed an independent estimate of its mass. From an evolutionary point of view, Pollux appears to be an intermediate-mass star (A. P. Hatzes et al. 2012; M. Aurière et al. 2015) that evolved past the Hertzsprung gap and is either at the base of the RGB or at the red clump.[4] Combining the long rotation period with estimates of the convective turnover timescale in the convective envelope of evolutionary models for Pollux, its Rossby number should be $Ro \approx 2$. This is larger than the classical $Ro_{\rm max} = 1$ value characteristic of stars in the magnetic instability strips where the $\alpha-\Omega$ dynamo process is expected to be active and to generate the observed surface magnetic field (C. Charbonnel et al. 2017; M. Aurière et al. 2021). Pollux thus lies slightly outside the trends connecting B_ℓ, Ro, and $P_{\rm rot}$, which raises the question of the origin of the sub-gauss level surface magnetic field detected in this very slowly rotating giant star and other giants of its class.

Three-dimensional magnetohydrodynamical (MHD) numerical simulations of the envelopes of red giant stars, constrained by results from spectropolarimetry on the field strength and configuration of the surface magnetic field, are the best way to explore and study the possible origin of this field. Despite only being a numerical representation of real stars, these simulations are extremely useful tools for understanding the complex nonlinear dynamics occurring within stars, especially when they can be constrained by observations. The number of such published numerical experiments, however, is very small, and few works have been devoted to the three-dimensional numerical simulation of the convective envelopes of red giant stars (A. S. Brun & M. K. Browning 2017; P. J. Käpylä et al. 2023). Global 3D hydrodynamical simulations of convection in red giant stars reveal large convective cells and a dominant dipolar flow in both nonrotating (D. H. Porter et al. 2000; P. R. Woodward et al. 2003) and rotating (A. Palacios & A. S. Brun 2007; A. S. Brun & A. Palacios 2009) configurations. Recently, 3D hydrodynamical simulations of the lower convective envelope and the radiative interior of a red giant were used to study the generation and propagation of internal gravity waves in these stars with the `PPMstar` code (S. Blouin et al. 2023). Other 3D simulations of these stars include 3D radiation hydrodynamics simulations of portions of the envelope coupled with the atmosphere of RGB and AGB stars (see A. Chiavassa et al. 2024, for a recent review). Regarding MHD simulations, only two studies so far relate to late-type stars: (1) the work by S. B. F. Dorch (2004), where they studied the red supergiant Betelgeuse and found three different modes of dynamo in their simulation, with a saturated nonlinear mode operating at twice the equipartition level, and (2) our preliminary 3D MHD anelastic simulation of Pollux with the ASH code (A. Palacios & A. S. Brun 2014), in which we explored the evolution of a multipolar magnetic seed in the rotating convective envelope of the star. In that preliminary study, the possibility for a dipolar field of a few gauss to emerge from a multipolar magnetic seed was emphasized.

In the present paper, we build on this preliminary simulation and present three 3D MHD simulations with which we explore the parameter space and its impact on the dynamo that develops in the extended convective envelope of a slowly rotating giant like Pollux. In Section 2 we describe our numerical setup and the adopted parameters. In Section 2.5, we analyze the hydrodynamic behavior of the simulations. In Section 3, we first tentatively compare the results of our simulations with the observational characteristics of the surface magnetic field of Pollux derived from the spectropolarimetric monitoring of this star published by M. Aurière et al. (2021). Also in that section, we analyze the dynamo regimes obtained and discuss them as a function of the parameters used. Finally we discuss our results and conclude in Section 4.

[4] The position of the star in the H-R diagram does not allow us to disentangle its actual evolutionary status.

2. Numerical Setup

In this section we describe the main elements of the ASH code (T. Clune et al. 1999; A. S. Brun et al. 2004), as well as the specific boundary and initial conditions we used for our numerical model.

2.1. Set of Equations

We want to understand the dynamo action that takes place in the convective envelope of a slowly rotating red giant. To do so, we use the ASH code, which solves the 3D MHD anelastic set of equations using a pseudo-spectral method. The anelastic approximation allows the simulation to account for the effects of density stratification, and to avoid capturing sound waves that would strongly limit the time step. The background density $\hat{\rho}$, the entropy $\hat{S}$, the pressure $\hat{P}$, and the temperature $\hat{T}$ are linearized, with their fluctuations indicated respectively as ρ, S, P, and T.

The equations solved by ASH are

$$\boldsymbol{\nabla}\cdot\hat{\rho}\,\boldsymbol{v}=0,\ \boldsymbol{\nabla}\cdot\boldsymbol{B}=0 \tag{1}$$

$$\hat{\rho}\left(\frac{\partial \boldsymbol{v}}{\partial t}+(\boldsymbol{v}\cdot\nabla)\boldsymbol{v}+2\boldsymbol{\Omega}_*\times\boldsymbol{v}\right)=-\nabla P+\rho\boldsymbol{g} +\frac{1}{4\pi}(\nabla\times\boldsymbol{B})\times\boldsymbol{B}+\nabla\cdot\mathcal{D} \tag{2}$$

$$\hat{\rho}\,\hat{T}\frac{\partial S}{\partial t}=-\hat{\rho}\,\hat{T}\boldsymbol{v}\cdot\nabla(\hat{S}+S)-\boldsymbol{\nabla}\cdot\boldsymbol{q}+\Phi_d+\hat{\rho}\,\varepsilon \tag{3}$$

$$\frac{\partial \boldsymbol{B}}{\partial t}=\boldsymbol{\nabla}\times[\boldsymbol{v}\times\boldsymbol{B}-\eta\boldsymbol{\nabla}\times\boldsymbol{B}], \tag{4}$$

with g the magnitude of the gravitational acceleration, $\boldsymbol{v}=v_r\hat{\boldsymbol{e}}_r+v_\theta\hat{\boldsymbol{e}}_\theta+v_\varphi\hat{\boldsymbol{e}}_\varphi$ the velocity field, $\boldsymbol{B}=B_r\hat{\boldsymbol{e}}_r+B_\theta\hat{\boldsymbol{e}}_\theta+B_\varphi\hat{\boldsymbol{e}}_\varphi$ the magnetic field, and $\boldsymbol{\Omega}_*=\Omega_*\hat{\boldsymbol{e}}_z$ the angular velocity around the rotation axis z. The volumetric heating term ε approximately represents the heating associated with the nuclear reactions in the stellar core. It is estimated as $\varepsilon=\varepsilon_0\hat{T}^{n_c}$. In our case of modeling the convective envelope of a red giant, we set $\varepsilon_0=0$ since the hydrogen-burning shell is deeper in the radiative core.

We define the viscous stress tensor $\boldsymbol{D}$ as

$$D_{ij}=2\hat{\rho}\,\nu\left[e_{ij}-\frac{1}{3}\boldsymbol{\nabla}\cdot\boldsymbol{v}\delta_{ij}\right] \tag{5}$$

with e_{ij} the stress tensor. The dissipation term Φ_d is described as

$$\Phi_d=2\hat{\rho}\,\nu\left[e_{ij}e_{ij}-\frac{1}{3}(\boldsymbol{\nabla}\cdot\boldsymbol{v})^2\right]+\frac{4\pi\eta}{c^2}\boldsymbol{J}^2, \tag{6}$$

with $\boldsymbol{J}=(c/4\pi)\nabla\times\boldsymbol{B}$ being the current density.

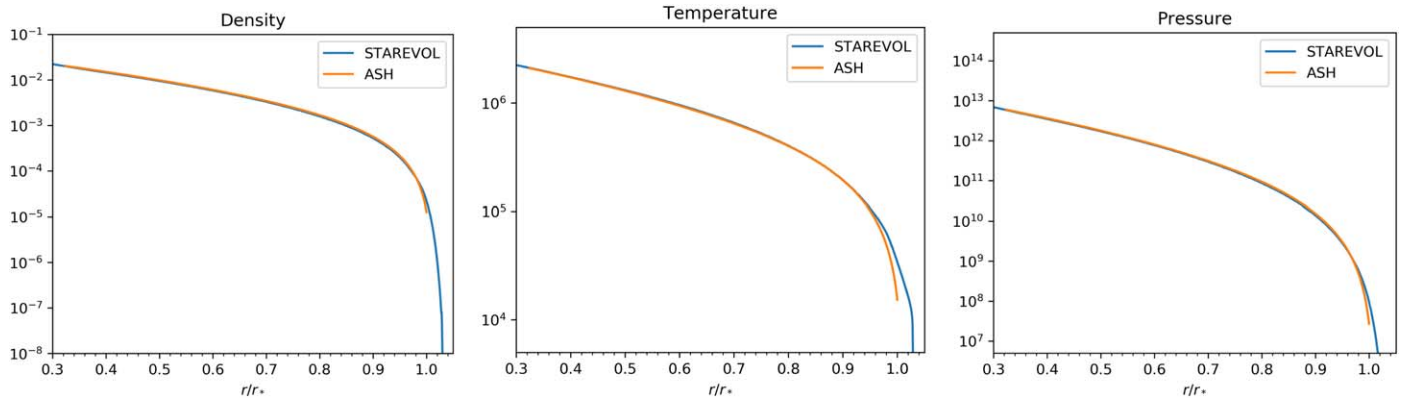

Figure 1. Comparison of the 1D profiles of density, temperature, and pressure (from left to right) with the spherically symmetric background profiles obtained in ASH.

We set the upper and lower boundaries as stress-free impenetrable walls with a constant entropy gradient; therefore following

$$v_{r_{\rm top},r_{\rm bot}} = 0 \tag{7}$$

$$\frac{\partial}{\partial r}\left(\frac{v_\theta}{r}\right)_{r_{\rm top},r_{\rm bot}} = \frac{\partial}{\partial r}\left(\frac{v_\phi}{r}\right)_{r_{\rm top},r_{\rm bot}} = 0 \tag{8}$$

$$\left(\frac{\partial \hat{S}}{\partial r}\right)_{r_{\rm top},r_{\rm bot}} = C_S, \tag{9}$$

with C_S a constant set to match the surface properties of the red giant. We explored two different types of magnetic boundary conditions to test their effect. In the first case (P2M2D), the magnetic fields at the upper and lower radial boundaries match a potential field, i.e., $B_r|_{r_{\rm top}} = B_r|_{r_{\rm bot}} = \nabla\Psi,\ \Delta\Psi = 0$. We follow the same upper magnetic boundary condition for P2M2 and P3M2 but consider instead a perfectly conducting lower radial boundary such that $B_r|_{r_{\rm bot}} = \frac{\partial}{\partial r}\left(\frac{B_\theta}{r}\right)_{r_{\rm bot}} = \frac{\partial}{\partial r}\left(\frac{B_\phi}{r}\right)_{r_{\rm bot}} = 0$. The latter condition favors horizontal fields close to the boundary.

2.2. Initial Model

In a similar fashion to A. S. Brun & A. Palacios (2009), we focus on the convective and magnetic properties of the red giant star, so we only model its extended convective envelope (about 70% of the stellar radius and 60% in mass) without treating the deep radiative interior. For the upper layers, we limit ourselves to 95% of the total radius for numerical purposes since the density drops sharply close to the surface.

We build the background of the simulation on a 1D structure computed with the evolution code STAREVOL (L. Amard et al. 2019; A. Palacios et al. 2006). It consists in a $2.5 M_\odot$ model evolved to the red giant phase up to a luminosity $L = 40\ L_\odot$ and a radius $R \sim 9\ R_\odot$, consistent with the observed properties of the star Pollux (M. Aurière et al. 2009, 2021). We set the rotation rate $\Omega = 1.28 \times 10^{-7}$ rad s^{-1} ($v \sin i \sim 1.3$ km s^{-1}), comparable to the observed rotation value. In Figure 1 we compare the profiles of density, temperature, and pressure obtained from 1D stellar models to the equivalents obtained with ASH after convergence. We use a Newton–Raphson solver to accommodate the differing equations of state (M. S. Miesch et al. 2000).

We focus on three models where the main differences are the value of the thermal diffusivity (the Prandtl number) and the initial magnetic configuration. P2M2 and P3M2 start with a weak multipolar magnetic seed, with P2M2 having a thermal diffusivity eight times larger than P3M2. P2M2D has the same properties as P2M2 but starts with a strong dipolar field and uses a potential match as its inner magnetic boundary condition, as opposed to a perfect conductor for the other two cases. The properties of the three models are described in Table 1. Note that we also explored cases with a lower magnetic Prandtl number. They are not shown here since they failed to build up a sustained dynamo action at the magnetic Reynolds number we were able to run as of today.

The models are computed with a numerical resolution $N_r \times N_\theta \times N_\phi = 256 \times 512 \times 1024$. Note that in this version of ASH, the variables are expanded along the spherical harmonics $Y_l^m(\theta, \phi)$ in the horizontal directions and the Chebyshev polynomials $T_n(r)$ for the radial points.

In this work we did not explore the effect of changing the resolution nor the level of turbulence by varying the diffusivities proportionally. This has previously been shown in the case of similar simulations by A. S. Brun & A. Palacios (2009), where they test two different resolutions and levels of turbulence for each case they study. They show that the large-scale circulations are maintained and that the global dynamics remains broadly the same.

Table 1 also summarizes the characteristic dimensionless numbers of each model. The Rayleigh numbers are high enough that convection can be triggered (C. A. Jones et al. 2009; S.-i. Takehiro et al. 2020). P2M2D and P2M2 have very comparable values for their Reynolds, Rayleigh, Péclet, and convective Rossby numbers, as can be expected since they share the same hydrodynamic progenitor. The magnetic boundary conditions do not impact the convection directly; however, they have an impact on the dynamo and the global magnetic field. The models with a higher thermal diffusivity (P2M2, P2M2D) appear to be slightly more turbulent (with a higher Reynolds number), and their convective motions are also more affected by the rotation (lower convective Rossby number). The Péclet number is obviously larger for P3M2 since the thermal diffusivity is decreased, indicative of a more turbulent transport of heat by the convective motions.

2.3. Energetic and Convective Properties of Pollux

The distribution of energies in the different models averaged over time is presented in Table 2, while the temporal evolution of the various components of the volume-averaged kinetic energy is presented in Figure 2 for the P3M2 case. The kinetic

Table 1
Initial Properties of the Three Models

Surname	P2M2D	P2M2	P3M2
N_r, N_θ, N_ϕ	256, 512, 1024	256, 512, 1024	256, 512, 1024
$B_{\rm init}$ (G), l, m	10, 1, 0	1, 10, 7	1, 10, 7
Bot. mag. cond.	Pot. Match	Perf. Cond.	Perf. Cond.
ν_t	2.5×10^{14}	2.5×10^{14}	2.5×10^{14}
κ_t	2.0×10^{15}	2.0×10^{15}	2.5×10^{14}
η_t	1.25×10^{14}	1.25×10^{14}	1.25×10^{14}
Pr	1/8	1/8	1
Pm	2	2	2
Ta	1.08×10^6	1.08×10^6	1.08×10^6
Re	381	394	300
Ra	1.64×10^5	1.71×10^5	10.7×10^5
Pe	47.7	49.2	304
Ro_c	1.02	1.00	1.21
$\Delta\Omega_{75}$	1.07	1.20	1.52

Note. We show the numerical resolution, the initial surface magnetic strength, the magnetic boundary condition at the bottom of the simulation (potential match or perfect conductor), the surface kinetic viscosity ν_t, the surface thermal diffusivity κ_t, and the surface thermal diffusivity κ_t. In addition we summarize their characteristic dimensionless numbers estimated at mid-layer depth and averaged temporally: the Prandtl number $Pr = \nu/\kappa$, the magnetic Prandtl number $Pm = \nu/\eta$, the Reynolds number $Re = \tilde{v}D/\nu$ with $\tilde{v}$ the rms velocity, the Rayleigh number $Ra = (-\partial\bar{\rho}/\partial S)\Delta S g D^3/(\bar{\rho}\nu\kappa)$, the Taylor number $Ta = 4\Omega^2 D^4/\nu^2$, the Péclet number $Pe = RePr$, and the convective Rossby number $Ro_c = \sqrt{Ra/(TaPr)}$. $\Delta\Omega_{75}$ gives the differential rotation expressed as $\Delta\Omega = (\Omega(\theta = 75°) - \Omega_{\rm eq})/\Omega_{\rm eq}$ with $\Omega_{\rm eq}$ the rotation at the equator.

Table 2
Energy Properties of the Three Simulations Averaged over Volume and Time after Dynamo Saturation

Name	P2M2D	P2M2	P3M2
KE (10^6 erg cm^{-3})	2.22	2.13	1.64
DRKE (% KE)	8.0	7.02	17.3
CKE (% KE)	86.9	88.5	78.3
MCKE (% KE)	5.1	4.5	4.4
ME (% KE)	7.59	7.94	2.36
TME (% ME)	2.75	2.74	2.04
PME (% ME)	2.48	1.95	1.71
FME (% ME)	94.8	95.3	96.2

Note. The kinetic energy (KE) is broken down into an axisymmetric component associated with the differential rotation (DRKE), a nonaxisymmetric convective contribution (CKE), and the contribution from the meridional circulation (MCKE), and compared to the relative magnetic energy (ME). The latter is then divided into its axisymmetric toroidal (TME) and poloidal (PME) components, and a fluctuating (FME) nonaxisymmetric component.

energy (KE) can be divided into its components associated with the meridional circulation (MCKE), the differential rotation (DRKE), and the nonaxisymmetric convection (CKE; A. S. Brun & J. Toomre 2002).

First, in all cases, most of the kinetic energy goes into the nonaxisymmetric convective motions (CKE), with less kinetic energy stored in the axisymmetric differential rotation, and a weak meridional circulation. In the low-Pr simulations P2M2 (D), the energy preferentially goes into the convection compared to P3M2, but with less energy stored in the axisymmetric differential rotation. The meridional circulation

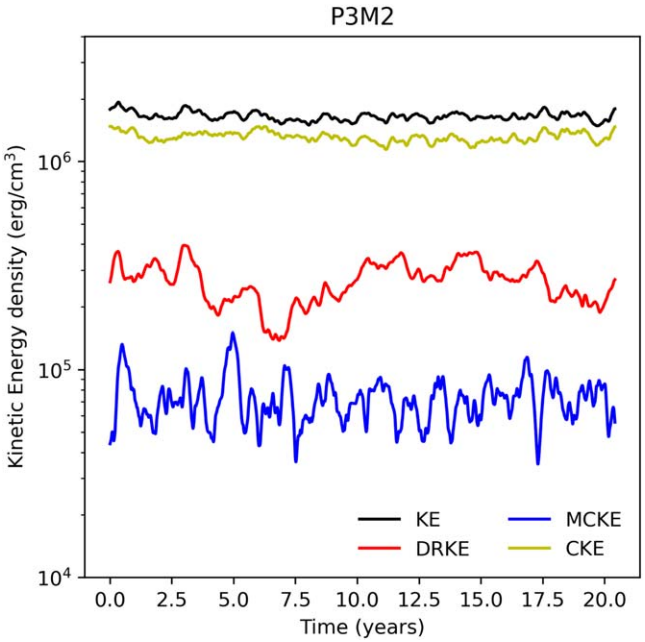

Figure 2. Evolution of the energies for the P3M2 models. The total kinetic energy (KE) is shown in solid black, its component associated with the differential rotation (DRKE) is in red, the one associated with the meridional circulation (MCKE) is in blue, while the energy carried by the convective motions (CKE) is in dark yellow.

is very comparable in the two cases. Once again, for the hydrodynamic part, P2M2D and P2M2 have similar energetic properties since they share the same hydrodynamic progenitor.

The most noticeable difference comes in the amount of magnetic energy that the simulations have developed. While the nonaxisymmetric fluctuating component of the magnetic energy remains largely dominant in the three simulations, the magnetic energy relative to the kinetic energy is three times lower in the high-Pr case (P3M2). This is indicative of a less efficient dynamo engine and will be discussed in Section 3. The mean ME is of the order of 2% in the two simulations. The toroidal and poloidal magnetic energies are almost equal, which is probably because the Ω-effect is very small; therefore this is more likely an α^2 dynamo than an α–Ω dynamo.

The convection is triggered by assuming an initial negative entropy gradient in the whole domain ($d\bar{S}/dr = -3 \times 10^8$) and by introducing random entropy perturbations. The convective overturn timescale taken at the middle of the convective envelope is between 200 days for P2M2(D) models and 230 days for P3M2, while the stellar evolution model gives 248 days, compared to the rotation period of 567 days. This leads to a stellar Rossby number $Ro_s = P_{\rm rot}/\tau_c \sim 2.28$, setting Pollux in the regime of slow rotation, where the convective motions are only weakly affected by the rotation. The fluid Rossby number as defined in A. S. Brun et al. (2017) is closer to 4.5 for the three models, therefore confirming that the simulation is dominated by the convection. It also means that the differential rotation is expected to be antisolar, with the equator rotating more slowly than the poles. This is discussed in the section on the large-scale flows and confirmed for all cases. It also fits with the kinetic energy of the simulation being dominated by the convective motions.

We present the radial energy flux balance reached by P2M2 and P3M2 cases in Figure 3. As expected, once the equilibrium

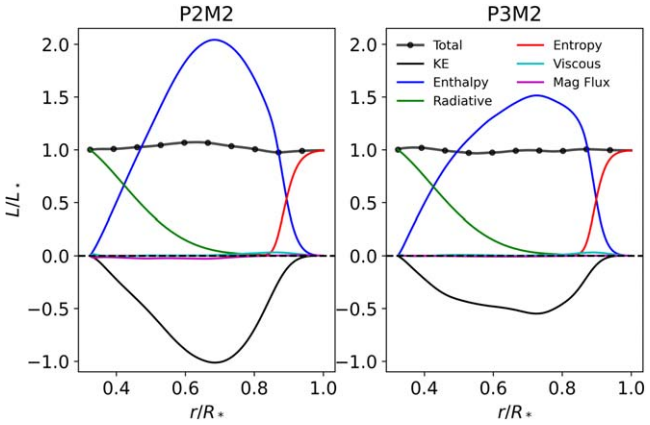

Figure 3. Radial energy flux balance averaged over six rotations for the P2M2 (left) and P3M2 (right) cases. The total luminosities (black with dots) are the sum of the kinetic energy (black), the enthalpy (blue), the radiative (green), the entropy (red), the magnetic (purple), and the viscous (cyan) fluxes. All values are normalized to the surface stellar luminosity.

is reached, the input energy is equal to the surface luminosity. In this figure we present the various fluxes transporting the energy through the star in the simulation.

The dominant feature in each simulation is the very high enthalpy flux rising to carry the energy outward, to counteract the negative flux of kinetic energy in the bulk of the convective envelope. However, this is also what distinguishes the two simulations: the low-*Pr* case (P2M2) presents an enthalpy flux that is about 30% more important, associated with a stronger convection (see P. J. Käpylä 2021, for a detailed analysis). The kinetic energy flux is therefore considerably higher (100% increase) to compensate for the larger enthalpy flux, and this will have important consequences for the internal dynamics that we will discuss in the following sections.

At the base of the simulations, the radiative flux dominates but shortly dies out, and confined to the surface layers is the entropy flux representing the flux carried by unresolved motions. Finally, the contribution of the viscous flux is almost negligible throughout the star.

2.4. Evolution of the Convective Motions

In Figure 4 we show on the left-hand side in five sequences the temporal evolution of the radial velocity close to the surface as a Mollweide projection for the P2M2 case over a period of 105 days. The right-hand side of the same figure shows the corresponding equatorial slices. As can be seen from each time frame, the convective flows emerge as large patches and dive down along very narrow concentrated lines. This forms very large convective cells at the top of the numerical domain, and the flows extend almost radially from the very top all the way to the bottom, maintaining a consistent structure throughout the whole domain. As examples, on the horizontal maps, we labeled two convective cells 1 and 2 that are characteristic of the dynamics. Cell 1 splits into two subcells (1a and 1b) because of the formation of a downflow lane in the middle, while cell 2 shrinks until the downflow lanes merge into one, leading to the disappearance of the cell. Such dynamics—the cleaving and merging of convective patterns—occurs continuously in the simulations. In the top left quadrant of the equatorial slices, we can observe a convective downflow growing and crossing the entire convective region as the convective cell passes through the equator. Note that the

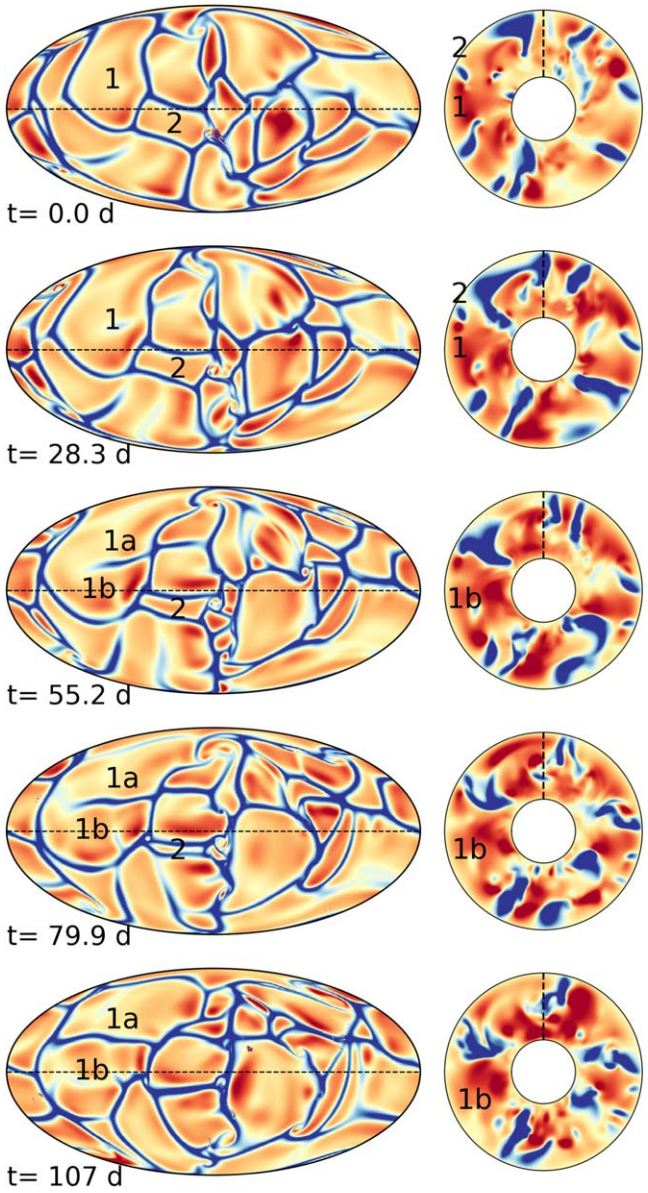

Figure 4. Left: maps showing the evolution of the surface radial velocity surface (Mollweide projection) for P2M2 cases through time. Upflows are colored in red and downflows in blue from velocities of −2000 to 2000 cm s^{-1}. The dashed line indicates where the equatorial cut is made. Right: equatorial slices at the corresponding time step displaying the radial velocity with a scale from −30,000 to 30,000 cm s^{-1}. The dashed line marks the center of the shell shown on the left. The time is indicated relative to the first frame taken arbitrarily close to the end of the simulation.

convective patterns are only mildly affected by the rotation. Considering the convective Rossby number presented in Table 1, the evolutionary timescale of the convective motions is of the order of the rotation period, therefore we should not expect to keep track of the structure over a rotation period.

Figure 5 presents shell and equatorial slices of the three simulations. This time, we display the shell slices at $R = 0.84R_*$, which corresponds to the maximal rms velocity in the three simulations. This illustrates the strongest flow in the convective domain, which can reach up to 400 m s^{-1}. We also present the temperature map. The convective structures look very similar to the ones observed in Figure 4 although they are deeper in the star (thus with higher velocities). Focusing on the top and bottom panels, we quickly notice that

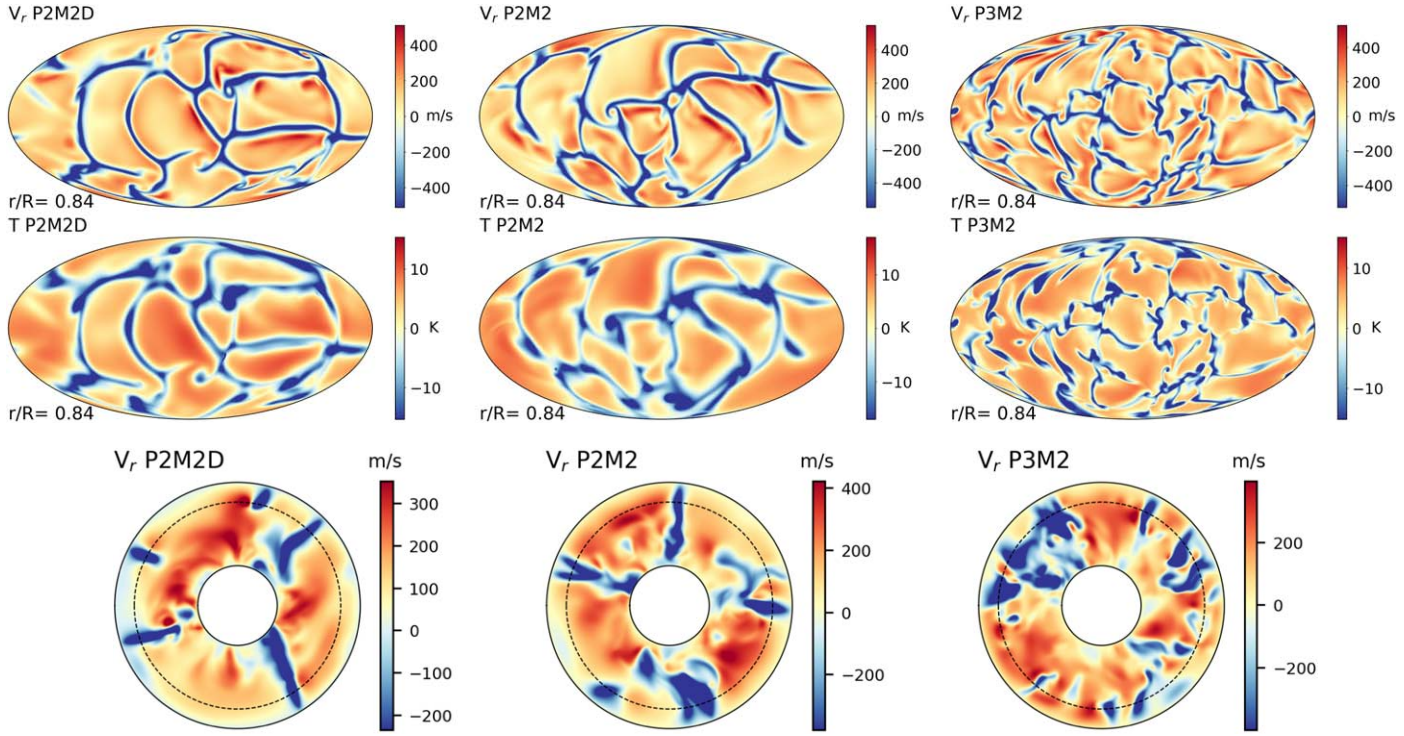

Figure 5. Top: radial velocity map at the peak of rms velocity at $R = 0.85R_\star$ (Mollweide projection) for the P2M2D, P2M2, and P3M2 cases (from left to right). Upflows are colored in red and downflows in blue. Middle: corresponding $T - \overline{T}$ maps with red (blue) colors indicative of a region that is hotter (colder) than average. Bottom: equatorial slices of the same model of each simulation showing the vertical velocity.

the high-*Pr* case (P3M2, lower κ_t) clearly shows smaller convective cells at the surface (see Figure 5). The convective patterns also appear to be busier and with smaller-scale modulations in the P3M2 simulation, although this is less clear on the equatorial slices. We find temperature differences up to 15 K locally. The The patterns observed on the radial velocity maps are also present on the temperature fluctuation maps. There is indeed a strong correlation between the hotter regions going outward and the colder regions going downward. This explains the high enthalpy flux we saw in Figure 3. In particular, note that this statement is true for all simulations despite the differences in *Pr* number between P2M2(D) and P3M2 cases. Finally, we can notice that, at the peak of the rms velocity, i.e., on the shell slices, the absolute values of the velocity and temperatures fluctuations are comparable in all simulations within 10%–15%.

2.5. Hydrodynamic Progenitor: Large-scale Flow

Figure 6 presents the differential rotation profile of P2M2 and P3M2 simulations averaged over the last 10 yr computed in the meridional plane. The two simulations show an antisolar differential rotation profile, in agreement with what is found in the case of solar-type stars with very large Rossby number (S. P. Matt et al. 2011; T. Gastine et al. 2014; A. S. Brun et al. 2022). The rotation profile is almost cylindrical with a faster rotating column joining the two poles through the fast stellar core.

The differential rotation between the poles and the equator is observed to be about twice as large in P3M2 as in P2M2. In the current case, we are dealing with a magnetic model where the quenching of differential rotation by the Lorentz force is to be accounted for. However, as is visible on the right panels of Figure 6 where we compare the hydrodynamic (dashed) and MHD (solid) radial cuts at given latitudes, the magnetic stresses did not change the rotation profiles of the simulations by much. Therefore, the differences between the two simulations have to come mainly from the large-scale hydrodynamic fluxes of angular momentum.

The rotation profiles are qualitatively similar to the RG1 case in A. S. Brun & A. Palacios (2009), which represents a red giant star with moderate rotation developing a cylindrical differential rotation in the envelope with a slowly rotating equator and fast rotating poles. They find in particular that the shape of the cylindrical profile is a consequence of the baroclinic torque being suppressed by the advection.

Since the angular momentum flux balance was already studied in depth in A. S. Brun & A. Palacios (2009), we leave the discussion to Appendix B for the three simulations. There we show the angular momentum flux balance for all simulations in Figure 17. In particular, we confirm that the magnetic torques are mostly negligible for all the studied cases compared to other transport mechanisms, even when starting with a strong dipole. We find that the meridional circulation responding to the Reynolds stress is mostly associated with the convective motion and the differential rotation, following the mechanism of gyroscopic pumping (M. S. Miesch et al. 2006; M. E. McIntyre 2007). We do see some contribution in the radial direction of Maxwell stresses transporting angular momentum inward. At the beginning of the simulation, the large-scale magnetic torque is very close to zero. This is consistent with the small axisymmetric field reported for PME and TME in Table 2.

In Figure 7, we show the meridional circulation cells driven in the three simulations. They are of similar strength but show slightly different patterns, in particular close to the surface. The simulations mostly have one large-scale meridional circulation

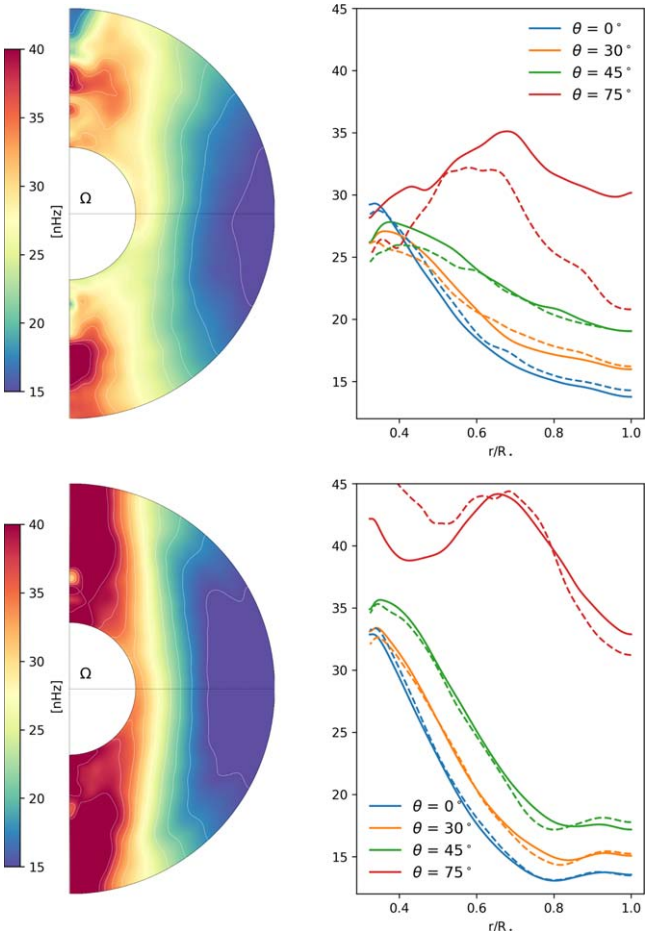

Figure 6. Differential rotation profile for the P2M2 (top) and the P3M2 (bottom) simulations integrated over 8 yr (about five rotation periods). On the left plots, we show colored contours of the angular velocity in the meridional plane. The color scale indicates the rotation rate in hertz, with slower (faster) rotation in blue (red). The rotation rate of the reference frame is $\Omega/2\pi = 19.8$ nHz. On the right panels, we present the radial profile of the angular velocity at different latitudes in the simulations. The dashed lines indicate the rotation profile attained by the purely hydrodynamic progenitors.

cell in each hemisphere bringing material, heat, and angular momentum from deep down to the surface at the equator, to restore the heat flux and angular momentum balance. However, the edges are not well defined, leading to the formation of a countercell of circulation below the surface where the meridional circulation is weakest. This is most visible in the case of P3M2.

A more detailed description of the thermal wind balance in the P3M2 case is presented in Figure 16 in Appendix A. In particular, we verify that the changes in v_ϕ globally correspond to the sum of all the contributing terms, which shows that the dynamic of the simulation reached an equilibrium. In agreement with A. S. Brun & A. Palacios (2009), we find that, due to the slow rotation, the baroclinic torque is suppressed by the advective flow, leading to the observed differential rotation.

3. Dynamo Field Generation in Pollux

3.1. Onset of Dynamo Action

The main novelty of these simulations is the addition of a magnetic field in the modeling of red giant stars. We first

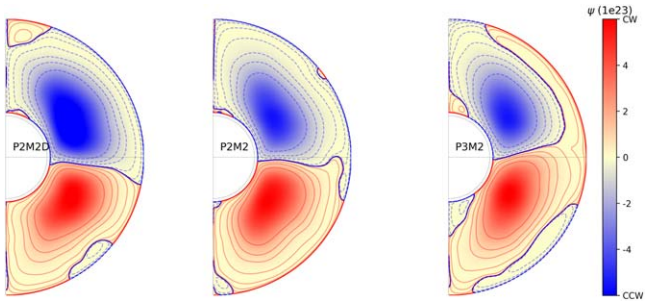

Figure 7. Meridional circulation for the three models. The color bar indicates the mass flux in g cm^{-2} s^{-1}, as well as the direction, with the blue region turning counterclockwise and the red region clockwise. The contours are drawn in geometric scale from $\pm 10^{23}$ to $\pm 10^{14}$.

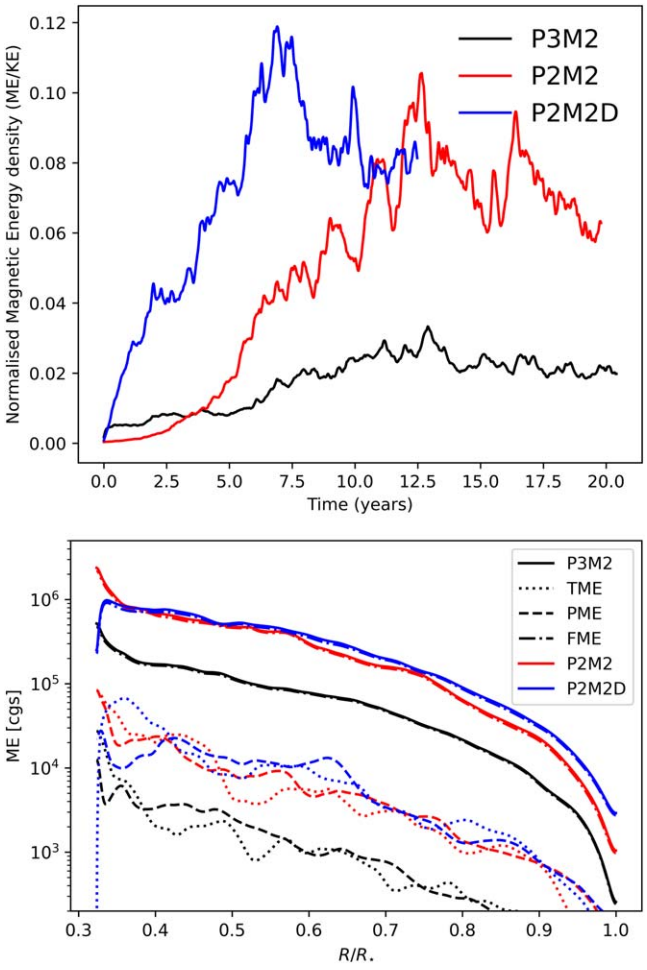

Figure 8. Top: volume-integrated magnetic energy normalized to the total kinetic energy for each model. Bottom: shell-averaged magnetic energies for the three models. The toroidal, poloidal, and fluctuating components are plotted as dotted, dashed, and dotted–dashed lines respectively.

verified that a dynamo could be set up by varying the magnetic diffusivity. We chose a magnetic Pr number ($Pm = \nu/\eta$) equal to 2 for the three cases, which allowed for a dynamo to build up and sustain over time.

In the top panel of Figure 8, we compare the temporal evolution of the magnetic energy relative to the kinetic energy of the three models to illustrate the growth of the dynamo converting kinetic energy (mostly from the convection) to magnetic energy.

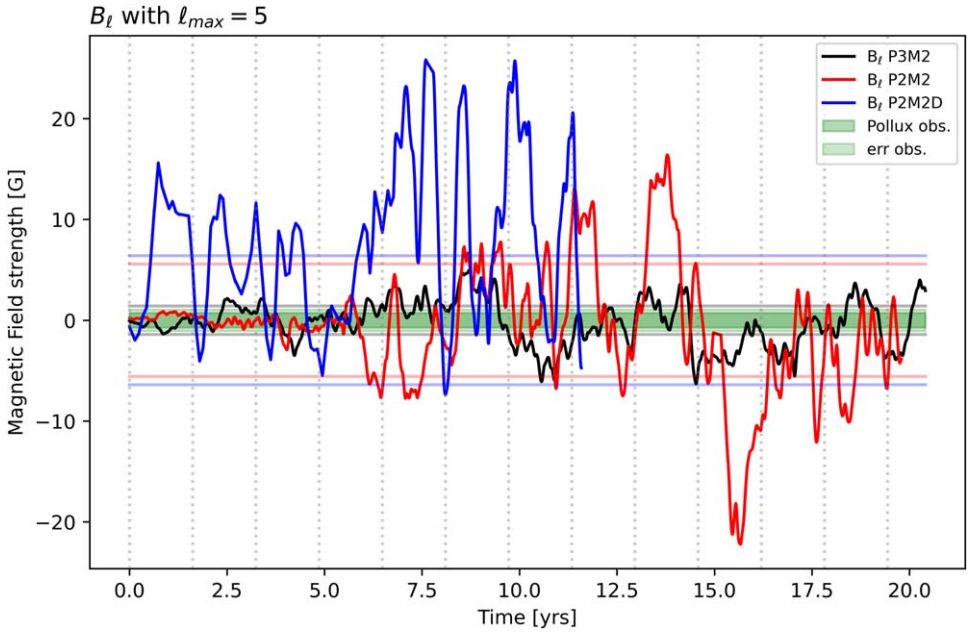

Figure 9. Surface-averaged longitudinal magnetic field filtered at $\ell_{\max} = 5$ as a function of time compared to the absolute maximal value observed in Pollux colored in green. The horizontal colored lines show the standard deviation of $|B_\ell|$ of each model. The vertical dotted lines indicate the rotation rate. We clearly see P3M2 is a convincing dynamo solution to explain Pollux's observed magnetism.

For the two cases starting with a weak multipolar field, the dynamo takes about 10–12 yr to saturate and to reach a regime of a statistically stationary state. This is much longer than the dipolar case (P2M2D), which saturates in about 7 yr. P2M2 and P2M2D reach a similar ratio ME/KE at saturation, despite different initial magnetic configurations. This first tells us that the dynamo engine is more dependent on the convective properties than on the initial field configuration if run long enough. Note that the small differences may also be due to the different magnetic boundary conditions at the bottom. Now, when comparing P2M2(D) and P3M2 simulations, the conversion to magnetic energy is about four times more efficient in the low-*Pr* models, with a mean ratio ME/KE going from 8% for P2M2 to 2% for P3M2. In particular, even though P2M2 and P3M2 have exactly the same initial setup except for their *Pr* number, the efficiencies of their dynamo engines appear to be quite different, and we will look for the underlying mechanisms in the following subsections.

The profiles of the magnetic energies and their components shown in the bottom panel of Figure 8 follow the density profile and scale in agreement with the evolution of the volume-averaged value of the magnetic energy (upper panel), with P3M2 being about 4–5 times smaller than the low-*Pr* cases. We decompose the magnetic energy into the axisymmetric part, itself split into the toroidal (TME) and poloidal (PME) components, and the fluctuating part (FME). There we can see that most of the magnetic energy is stored in the fluctuating part as detailed in Table 2. With the three solid lines, we also can see that the magnetic inner boundary conditions only have an effect very close to the bottom of the simulation. The matching to potential field forces the mean toroidal field to be null at the boundaries, as indicated by the dotted blue line dropping to zero close to the core.

We have now established that a self-sustained dynamo can be excited in simulations of the convective envelope of red giants. We will first have a look at the global field that can be produced and compare it to observations before describing the magnetic field properties in more detail.

3.2. Global Surface Field and Comparison to Observations

The first detection and analysis of the magnetic field of Pollux come from M. Aurière et al. (2009). They reveal a magnetic field with a magnitude less than 1 G. M. Aurière et al. (2015, 2021) refined the data and studied the geometry of this field; in the latter work they found it to be "mostly dipolar." We recall that the observations only cover about 5 yr of data and remain relatively sparse, therefore we can only compare the order of magnitude of the field at a given time. The field is so weak that the Zeeman broadening is hardly detectable, so the only measure that can be provided is a global measurement $B_\ell \simeq [-0.7, -0.1] \pm 0.3$. B_ℓ is defined in S. C. Marsden et al. (2014) as the mean longitudinal magnetic field, corresponding to the line-of-sight component of the stellar magnetic field integrated over the visible stellar disk.

In this section, and in particular in Figure 9, we want to compare our simulation to this observed quantity of Pollux. Since spectropolarimetric observations of Pollux do not capture small-scale features, we first apply a filter to the surface magnetic map of our simulation, and only keep $\ell \leqslant 5$ components. The resulting magnetic maps are presented in the second row of Figure 10. Second, we have to tilt our simulation using a coordinate transformation since Pollux was shown to be observed at an inclination of 10° with respect to the rotation axis. This may be of importance in particular for the low-order components of the magnetic field, which may be more intense closer to the pole. Finally, we compute the Cartesian B_x component of the magnetic field and integrate it over the visible surface to obtain B_ℓ. The results are shown for the three models in Figure 9, which shows the evolution of the magnetic field as well as its absolute standard deviation (after saturation). The average B_ℓ of the high-*Pr* P3M2 is close to the green region representing the observations with $\langle |B_\ell| \rangle \simeq 2.1$ G.

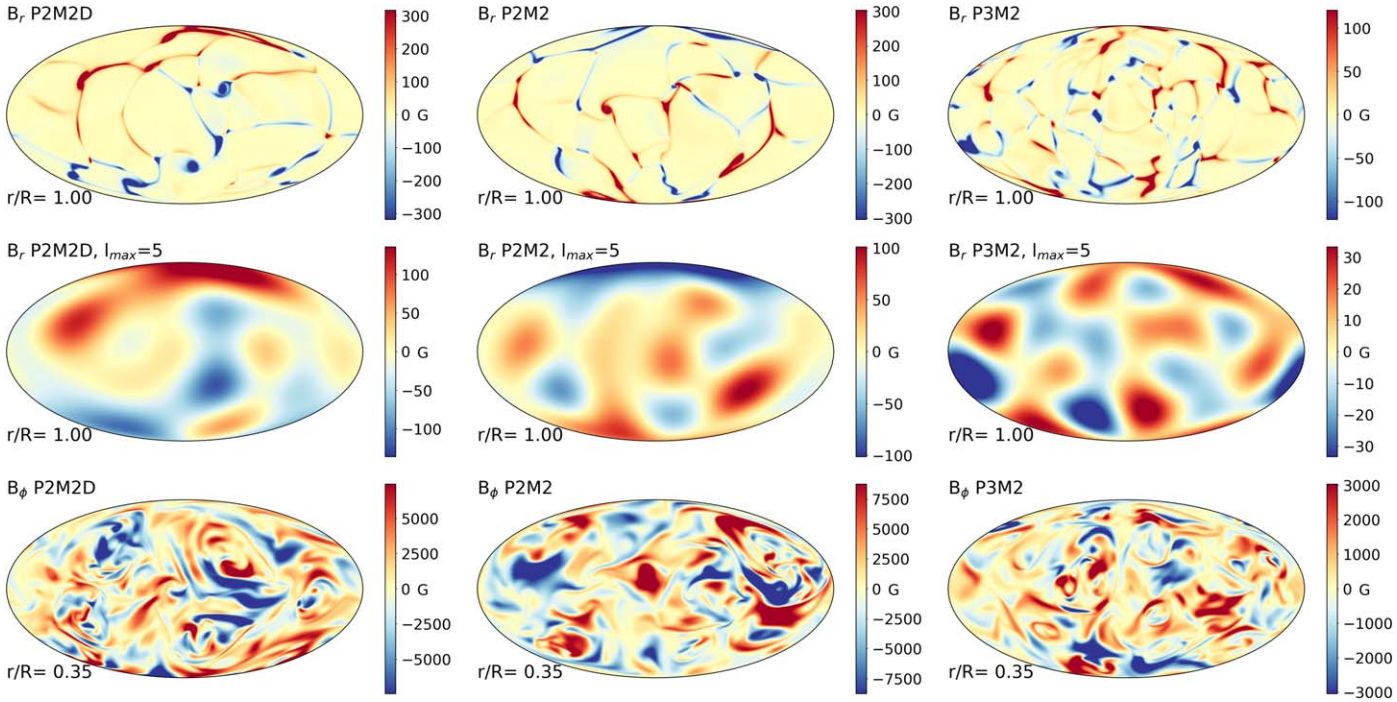

Figure 10. Top: intensity of the radial component of the magnetic field at the surface of the three cases. Middle: same plot showing only the components $\ell \leqslant 5$, comparable to what would be obtained from observations. Bottom: intensity of the azimuthal component of the magnetic field taken just above the base of the convective region. The snapshots correspond to the same time as in Figure 5.

This suggests that P3M2 may be a good representation of the type of dynamo existing in Pollux. In comparison, the two P2M2(D) simulations present a magnetic field with mean $|B_\ell|$ equal to 6.7 and 7.2 G for P2M2 and P2M2D, respectively, which is much stronger than what the observational uncertainty allows.

It is interesting to notice that, on one hand, the two simulations starting with a small-scale field show various changes of sign on relatively short timescales (1–2 yr) over the course of their evolution. While this is not observed in the data by M. Aurière et al. (2021), it is not incompatible. On the other hand, P2M2, which started with an initially strongly dipolar field, keeps an average magnetic field with the same sign for the full simulation. B_ℓ of the two P2M2(D) cases oscillates between strong and weak values on a timescale slightly different from the rotation period (more evident in the case of P2M2 shown in red). Therefore the periodicity may be associated with strong magnetic patches at the surface periodically reappearing. The period of variation is less obvious for P3M2, which seems to have multiple periods, likely associated with the surface convective motions, the rotation, as well as possible large-scale magnetic field reversal.

Overall, P3M2 is thus a very interesting dynamo simulation of Pollux as it shows a large-scale field compatible with observations. We will now turn to explaining the differences between the two dynamo simulations and why P3M2 is likely a better realization of the RGB star Pollux.

3.3. Properties of the Magnetic Field

In the first row of Figure 10 we show the radial field map near the top of the domain. We find very similar patterns to the radial velocity map, with the downflow lanes concentrating the radial magnetic field, leading to a strong field concentration at the interstices, up to 300 and 100 G for P2M2 and P3M2, respectively. The magnetic field is much lower in the center of the convective cells, generally below 10 G. Therefore, as the convective cells are smaller, P3M2 displays more complex magnetic patterns of lower intensity than P2M2. This apparently more complex field is confirmed by the filtered map shown in the middle row of Figure 10. In these plots, we tried to estimate the best magnetic maps that could be reconstructed from spectropolarimetric observations by applying a low-pass filter, only keeping the largest scales (with degrees of spherical harmonics up to 5 as in N. Bessolaz & A. S. Brun 2011, for example). Note that filtering the signal reduces by a factor of three the intensity of the tight magnetic ridges visible on the upper panels. We find P3M2 to be spotted with no clear large-scale field appearing, while P2M2 shows signs of a large-scale polarity, its north pole being strongly negative in that snapshot. The large-scale field components are discussed in more detail in the next subsection.

We now turn to the bottom panels of Figure 10, which present the azimuthal field close to the base of the convective region where the large-scale toroidal magnetic field is generally produced in solar-type dynamos (M. K. Browning et al. 2006). On this plot we find much more complex structures than in the upper layers, and at this depth the three simulations show the same complexity of patterns. Note, however, that the intensity of the field of P2M2 reaches 8000 G at the base of the convective region; this is twice as large as with P3M2, which peaks at 3000 G. This is still in agreement with what we saw in the ME profiles in Figure 8.

Figure 11 shows the radial and azimuthal components of the magnetic field in the equatorial plane, and we can see that the magnetic field is more intense closer to the bottom of the convective region, in agreement with Figure 8, and because of the turbulent pumping of the field by the strongest downflow. In particular, in the case of the low-*Pr* model P2M2, the

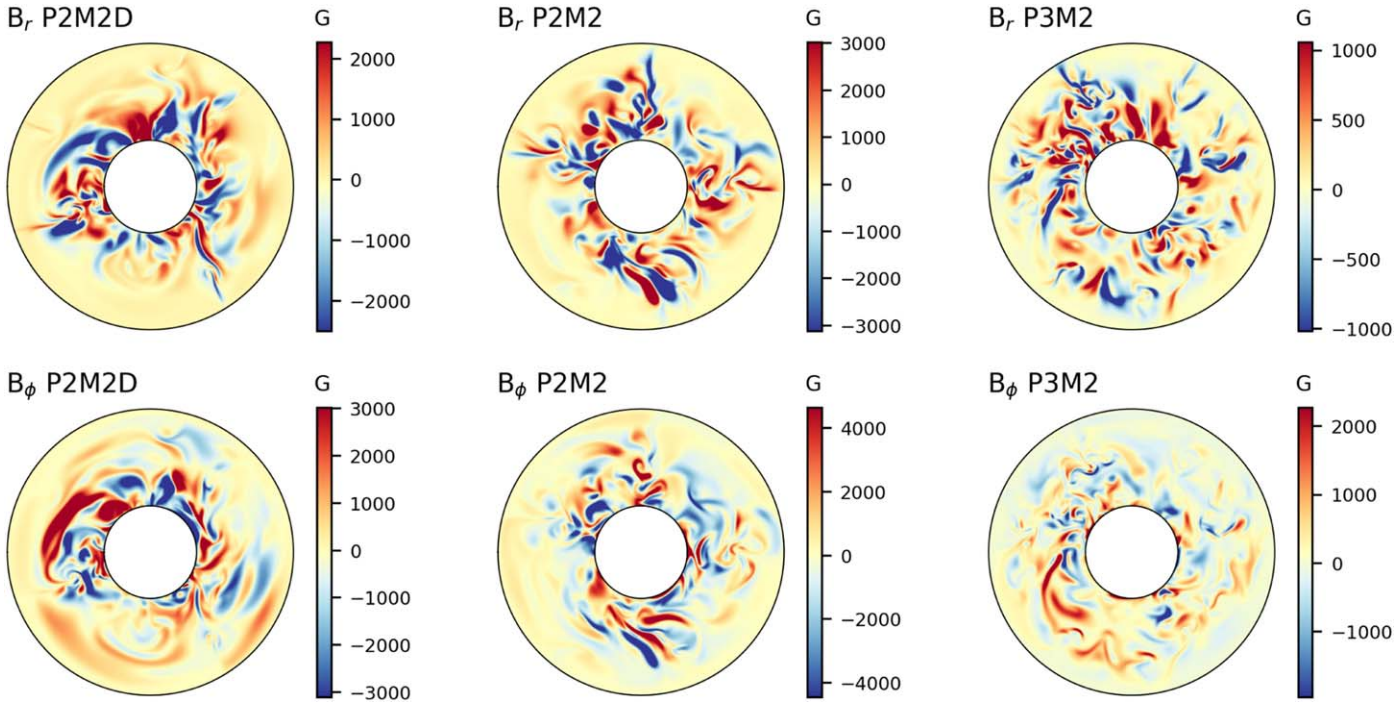

Figure 11. Equatorial slices displaying the radial (top) and azimuthal (bottom) components of the magnetic field for the three models. The snapshots correspond to the same time as in Figure 5. We note the complex mixing of field polarity and the more intense amplitude closer to the bottom of the domain.

regions with a strong radial field correspond to the downflow lanes seen on the surface maps of Figure 5. We notice, however, that well defined downflow lanes are not as visible on the equatorial plane slices when looking at the magnetic field. The structures are more complex but can still be traced back on the B_r panels, extending radially from the surface to the core, much less in the case of B_ϕ.

The 3D rendering of the radial velocity is illustrated in Figure 12 for the P3M2 case at 17 yr in the simulation. This figure is to be compared with the surface and equatorial slicing shown in Figure 5. There we clearly see convective cells rising and merging in downflow lanes from the surface to the center of the simulation. We also draw a potential extrapolation of the surface magnetic field, showing the complexity and the nonaxisymmetry of the magnetic field, with loops closing on each hemisphere of the simulation.

Figure 13 shows the intensity of the azimuthally averaged near-surface radial field as a function of latitude and time, also known as a butterfly diagram in the case of solar-type stars showing cyclicity (P. Charbonneau 2005). Here, our three models show strong magnetic poles with a weakly magnetized equator. The top row corresponds to the low-*Pr* simulation starting with a strong dipolar field, P2M2D. It keeps a strong dipole for the 12 yr of the simulation, and does not change sign, in agreement with what we saw in Figure 9. The two other cases start with the same weak small-scale field, therefore the large-scale magnetic structure has to build through the tryadic interactions leading to an inverse energy cascade as the simulation evolves (A. Strugarek et al. 2013). As observed in Figure 8, the dynamo engine takes about 10 yr to reach a state where stable large-scale structures can be built and sustained.

In Figures 8 and 10, we saw that P2M2 reaches a final state similar to P2M2D. However, as mentioned above, the dipole of case P2M2D is more clearly outlined in the top panel of Figure 10. This leads to a stronger azimuthally averaged field

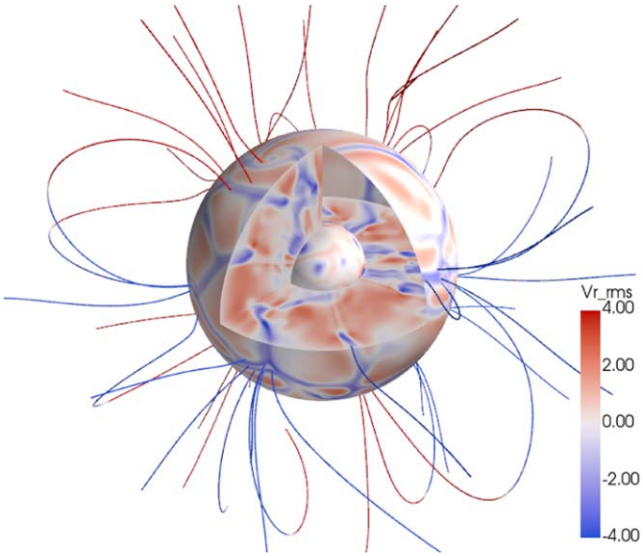

Figure 12. 3D representation of the radial velocity normalized to the local $v_{\rm rms}$ for the P3M2 case. Upflows are shown in red and downflows in blue. At the surface we extrapolated the magnetic field lines with a potential field source surface; they are colored with the radial component of the magnetic field strength.

compared to P2M2, where magnetic features of different polarities cancel each other. This is true despite the local magnetic field of each feature being of the same strength.

Nevertheless, the maximal intensity of the field displayed by P2M2 is still twice as large as with P3M2: 90 G for P2M2 and 45 G for P3M2. Globally, the patterns appear more intricate on P3M2 than on P2M2, happening on smaller spatial and temporal scales. Interestingly, both simulations show some reversals of the large-scale polarity, starting at about 14 yr for P2M2 and at 8 and 16 yr for the P3M2 case. This suggests that

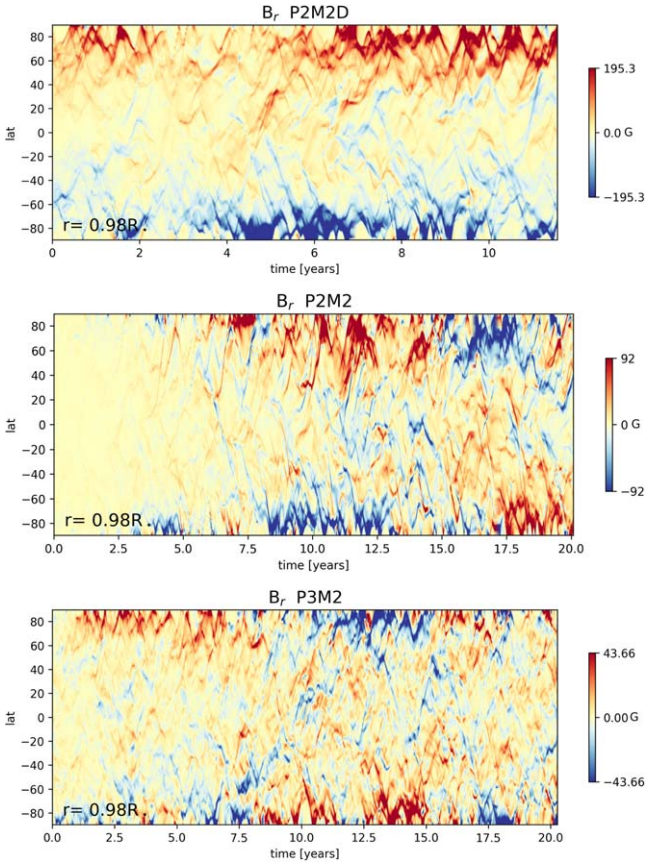

Figure 13. Time–latitude butterfly diagrams of the radial component of the surface magnetic field in the three cases.

global magnetic field reversal could be expected in red giant stars.

These features should also be observed in the large-scale components of the field of each simulation. In Figure 14 we compare the large-scale axisymmetric components of the magnetic field for the two models. The three simulations show multipolar fields with a mixture of symmetric and antisymmetric components, typical of a nonlinear dynamo that couples the two families (P. L. McFadden et al. 1991; M. L. DeRosa et al. 2012).

The larger dipole, quadrupole, and octupole of the P2M2(D) cases are in agreement with the larger magnetic energy than P3M2. This also confirms the qualitative trend we observed in Figure 13, and adds further support to the conclusion that the scale of the convective motions seems to connected to the scale of the magnetic field geometry. We come back to this point specifically in the next section.

It is interesting to verify that the dynamo of the P2M2 cases grows to produce $\ell = 2$ and $\ell = 3$ fields with a similar amplitude to the initial strong dipolar case (P2M2D) and varies on similar timescales. Their dipoles are a little different in the two situations. Although P2M2D started with a dipolar magnetic field and can reach a dipole stronger than 100 G, the initially multipolar case seems to build a field almost as strong, close to 70 G in absolute value. The main difference between the two models is that P2M2 seems to be more prone to global field reversal. Although the two simulations did not run for as long, P2M2D reached a stable configuration very quickly, and while the quadrupole flipped signs, the dipole and octupole remained in the same direction. This leads us to think that the global configuration of P2M2D may not change, and that the initial dipole is strong enough in P2M2D to influence the dynamo, even leading to an increase a little over the simulation. On the other hand, the large-scale fields of P3M2 are much smaller and do not compare. While the dipole seems to change sign only twice, the quadrupole seems to quickly oscillate around zero. When integrating B_r in one hemisphere, the polarity follows closely that of the dipole in all three cases.

3.4. Scales of the Dynamo Process

The differences in timescales and intensity of the surface radial field noticed in Figure 13 suggest that the convective properties also play a role in the large-scale field realized in our models. Additionally, the multiple timescales of B_ℓ variations seen in Figure 9 are likely connected to the timescale of the convective motions. Finally, as we saw in Figures 5 and 10, the regions of strong magnetic field are directly connected to the downflow lanes associated with the convection. S. M. Tobias & F. Cattaneo (2008) argued and showed that the scale at which the magnetic field is produced can be estimated from the velocity field scales. This would mean that the scale of the convection is directly connected to the scale of the dynamo and could explain the magnetic properties of our simulations.

To test this hypothesis and to better understand the generation of the large-scale magnetic field, we averaged the structure over a rotation period and computed the spectrum of the induction term following A. Strugarek et al. (2013) to reveal the dominant scales in the generation (or destruction) of magnetic features within the convective envelope. This involves decomposing both the velocity field and the magnetic field on a vectorial spherical harmonics basis ($\mathcal{R}_\ell^m$, $\mathcal{S}_\ell^m$, and $\mathcal{T}_\ell^m$) and computing the dominant term of the induction equation ($\nabla \times (\boldsymbol{U} \times \boldsymbol{B})$) for each ℓ and m component. We then summed over all $m \neq 0$ to obtain the nonaxisymmetric part of each spatial scale (the axisymmetric part being negligible). In Figure 15, we show the contribution of each spatial scale to the production and destruction of magnetic field at four depths in the two simulations. To better compare the features of the spectra from the two simulations, we normalized them to their absolute maximum. Note that the scales involved in these simulations are smaller (larger ℓ) than what is depicted in the solar case, as in A. Strugarek et al. (2013) for example. The two spectra are qualitatively very similar except at $r = 0.7R_\star$, where they are somehow opposite in sign. We find the magnetic field to be produced at the bottom and the top of the convective envelope, while the regions in between either create or destroy the magnetic features depending on the considered scale. Now, when comparing the simulations with different convective properties P2M2 and P3M2, all panels show the P2M2 case peaking at a lower ℓ than P3M2, indicative of larger scales being more efficient at producing or destroying magnetic structures. This is particularly visible in the rightmost panel closer to the surface, where P2M2 and P3M2 peak around $\ell \sim 3$ and $\ell \sim 9$, respectively. This is in agreement with what we qualitatively saw in Figure 13, where the large-scale components are much more pronounced on P2M2 plots than on P3M2's. Meanwhile the spectra are more alike closer to the bottom of the convective region. This is likely due to the similar patterns observed in the bottom panel of Figure 10 showing the azimuthal field. Hence P3M2 possesses a small B_ℓ because its convection and dynamo both operate at a smaller scale.

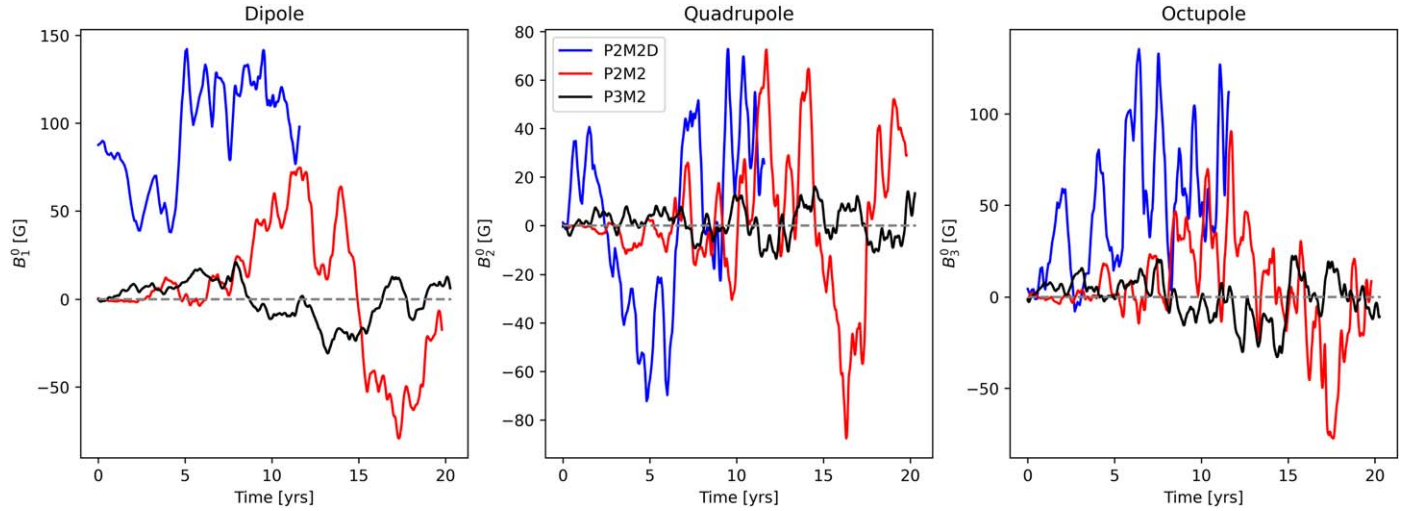

Figure 14. Large-scale axisymmetric components of the surface magnetic field as a function of time.

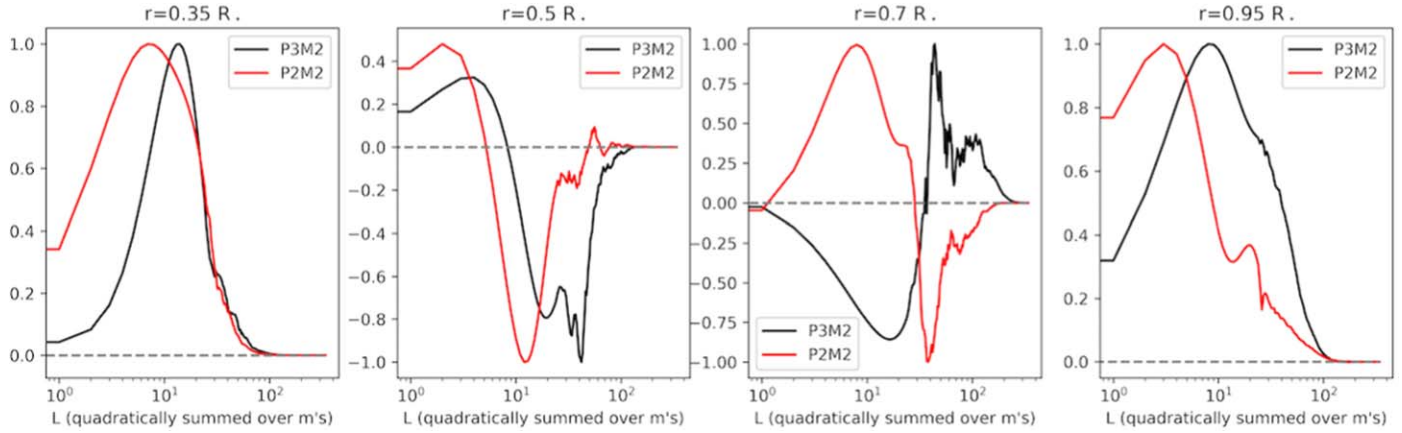

Figure 15. Spectra of the induction term normalized to their respective maximal absolute value, at four depths in simulations P2M2 and P3M2, averaged over a rotation period. Here it is clear that P3M2 operates at a smaller scale and thus generates a smaller large-scale field.

4. Discussion and Conclusion

In this study, we have sought to understand what happens to stellar magnetism in the post-main-sequence phase. Indeed, the star Pollux has been observed via ZDI techniques to possess a weak global magnetic field of the order of 1 G. Such magnetic fields are relatively weak when compared to many main-sequence stars of intermediate mass. We recall here that Pollux is a 2.5 $M_\odot$ RGB star. On the main sequence such massive stars are either highly magnetized in the Ap/Bp class, with field strengths reaching several kilogauss, or have undetectable fields (F. Lignières et al. 2014). The origin of the large-scale weak magnetic field of Pollux has no clear explanation. Hence, we need to understand whether the magnetic field of Pollux originates from the remnant of the convective core on the main sequence or if it is continuously generated by the action of an internal dynamo hosted in the extended convective envelope of the red giant. Despite the very large convective envelope, the presence of a dynamo engine sustained by the differential rotation and the large convective motions is very questionable because of the very slow rotation of red giants. MHD simulations are useful tools to study the dynamics of magnetized RGB stars provided that the analyses are performed keeping in mind that they are only numerical experiments and not real stars. That being said, in order to test the origin of a small global field in Pollux, we constructed three high-resolution MHD simulations of the convective envelope in a numerical setup as close as possible to Pollux using the ASH code (A. S. Brun et al. 2004), opening the way to modeling the magnetic field of red giant stars and understanding post-main-sequence stellar magnetism.

Two of the simulations differ in their initial Prandtl number, and the third one starts with different initial condition, testing the robustness of the results. We first showed that the large-scale hydrodynamic motions are only weakly affected by the presence of a magnetic field. We observed a cylindrical rotation profile that we linked to the balance between the angular momentum transport by the meridional circulation and the Reynolds stresses associated with the convection. The feedback from the Lorentz force is too weak to create a global torque that would efficiently modify the flow. The differences in Prandtl number between the two simulations, and in particular in thermal diffusivity, led to differences in the size of the convective patterns, with the simulation with a high thermal diffusivity (low Pr) having much larger convective cells. In both simulations, we found the strong correlation between the temperature and the convective motions to be the source of the large enthalpy flux. We also found a dipolar temperature structure because of the slow rotation, which was found in previous work for stars of this type.

The three models developed a complex dynamo mostly generated by small-scale fluctuating terms, leading in one case

to a weak surface magnetic field of the order of a few gauss when integrated over the visible disk. We verified that the onset of the dynamo was not dependent on the initial conditions by computing a simulation with different magnetic boundary conditions and initial magnetic seeds of different complexity and intensity. We found the simulation starting with a small-scale multipolar field to reach the same dynamo efficiency as the initially strong dipole, comforting us in the fact that we have a genuine dynamo. The ridges of the surface magnetic field are strongly aligned with the edges of the convective cells where the material falls inward. As a consequence of this correlation between the global convective properties and the surface field, we find that our two simulations with different convective properties have produced very different surface fields. We extracted the large-scale components of the magnetic field. The low-*Pr* case with large convective cells shows strong dipole, quadrupole, and octupole modes, while the model with smaller-scale convection presents weak large-scale components. Note that in the two cases, the dipole varies proportionally to the global field, changing sign as the simulations evolve. We explored the scale at which the magnetic field is being generated in each simulation. We showed that a large-scale convection more efficiently generates large-scale fields and vice versa by computing the spectrum of the induction term for each simulation.

Quantitatively, we found the simulation with small convective cells to have a mean azimuthal field $|B_\ell|$ of 2 G, close to the detected magnetic field $|B_\ell| = [0.1; 0.7]$ G. The two other simulations show a mean surface field around 7 G. Although they are a little too large to match the surface field of Pollux, these line up very well with all the other red giants' magnetic fields measured in M. Aurière et al. (2015), which are between 1.9 and 41 G[5] depending on their evolutionary stage. In addition, we recall that our simulations do not reach the exact surface of the star; the magnetic field strength of 2 G reported here is evaluated near the top of the domain. Based on the radial distribution of the field (Figure 8), it is possible that the field could be even closer to the observed value. Nevertheless, we are encouraged by our finding that small-scale convection may explain the low value of the azimuthally averaged magnetic field of Pollux measured by M. Aurière et al. (2021). Interestingly, the simulations show several reversals of the field over the 20 yr computed, leading us to think that this feature could be detected if the star is observed long enough. We therefore encourage regular monitoring of red giants like Pollux in the search for a possible magnetic field reversal.

Acknowledgments

We would like to thank the referee for the relevant comments that improved the quality of the manuscript. We acknowledge financial support by CNES PLATO grant and by ERC Whole Sun project 810218. These simulations have been computed on GENCI supercomputers at Idris and TGCC centers through project 1623. L.A. would like to thank A. Finley, Q. Noraz, and A. Strugarek for their help with 3D projections and helpful discussions.

Appendix A
Thermal Wind Balance

Figure 16 shows a two-dimensional reconstrution of the components of the wind balance for the P3M2 case. The detailed description of each term can be found in A. Strugarek et al. (2011)

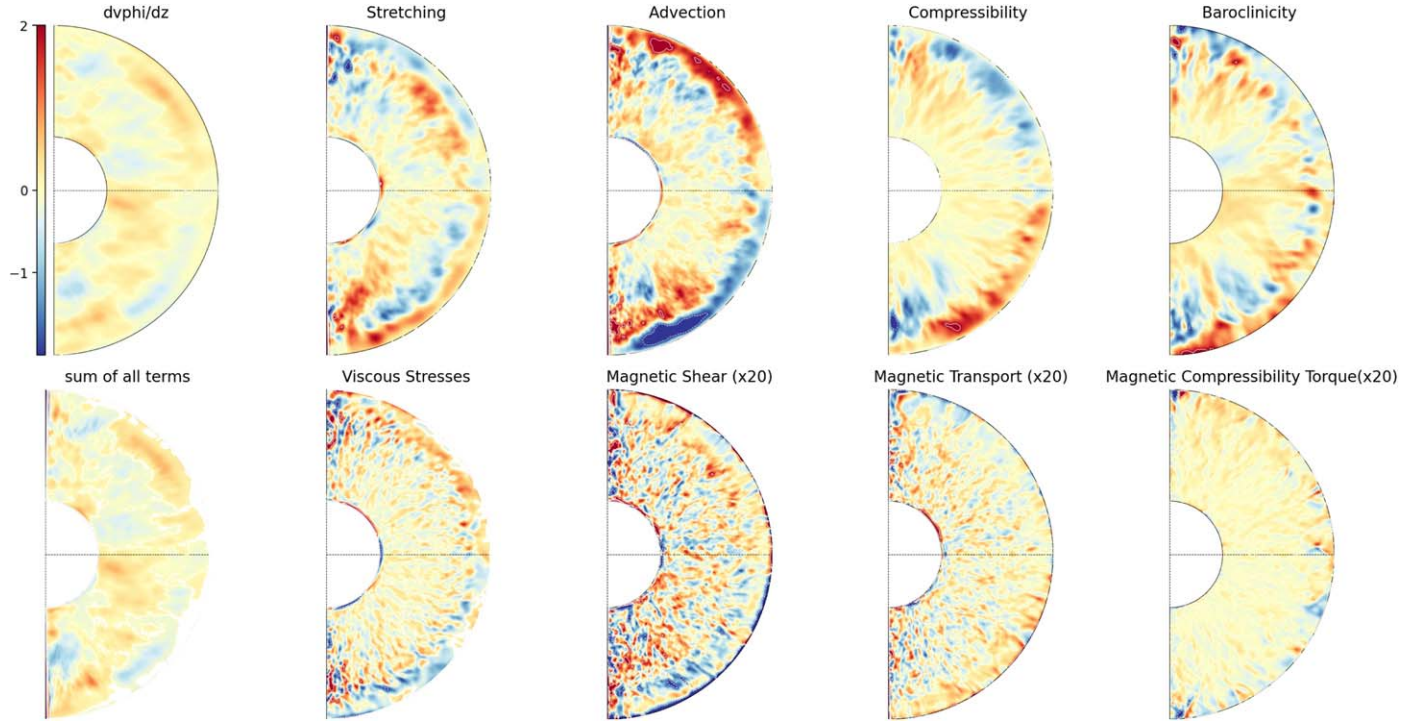

Figure 16. 2D reconstruction of the thermal wind balance in the P3M2 model averaged over 8 yr (∼5 rotation periods). Note that the magnetic components in the three bottom right panels have been increased for visualization purposes.

[5] Except for EK Eri, which is known to be overactive with a magnetic field close to 100 G. It is thought to originate from a magnetic Ap star (see M. Aurière et al. 2011).

or A. S. Brun et al. (2022). Note that in order to visualize correctly the contribution of all terms, we had to increase by a factor 20 the contributions from magnetic components. The overall magnetic contribution is thus very small. The two main mechanisms at work balancing each other are mostly the advection and the compressibility terms.

The other cases have a very similar thermal wind balance, the only noticeable difference being the contribution of the magnetic terms, although this is still negligible.

Appendix B
Angular Momentum Flux Balance

We compute the angular momentum flux balances for the two main cases, the results are displayed in Figure 17. The definitions of the different terms come from A. S. Brun et al. (2004), with the slight difference that the meridional circulation term is split into two parts: one that is associated with the mean latitudinal flow and one that is linked to the rotation, more specifically

$$\boldsymbol{F}^{\rm RSC} = r\sin\theta\rho(\langle v'_r v'_\phi\rangle\vec{e_r} + \langle v'_\theta v'_\phi\rangle\vec{e_\theta}) \quad \text{(B1)}$$

$$\boldsymbol{F}^{\rm RSDR} = \rho\langle\vec{v}_M\rangle r\sin\theta\langle v_\phi\rangle \quad \text{(B2)}$$

$$\boldsymbol{F}^{\rm C} = \rho\langle\vec{v}_M\rangle(r\sin\theta)^2\Omega_0 \quad \text{(B3)}$$

$$\boldsymbol{F}^{\rm VD} = -\nu\rho r^2\sin\theta\left[\partial_r\left(\frac{\langle v_\phi\rangle}{r}\right)\vec{e_r} + \frac{\sin\theta}{r^2}\partial_\theta\left(\frac{\langle v_\phi\rangle}{\sin\theta}\right)\vec{e_\theta}\right] \quad \text{(B4)}$$

$$\boldsymbol{F}^{\rm MS} = -\frac{r\sin\theta}{4\pi}(\langle B'_r B'_\phi\rangle\vec{e_r} + \langle B'_\theta B'_\phi\rangle\vec{e_\theta}) \quad \text{(B5)}$$

$$\boldsymbol{F}^{\rm MT} = -\frac{r\sin\theta}{4\pi}\langle B_\phi\rangle\langle\boldsymbol{B}_M\rangle \quad \text{(B6)}$$

for the Reynolds stresses associated with convection (RSC) and differential rotation (RSDR), the components associated with the Coriolis force (C) and the viscous diffusion (VD), the magnetic stresses (MS), and the magnetic torque (MT), respectively. $\boldsymbol{v}_M$ and $\boldsymbol{B}_M$ indicate the meridional components of the velocity and of the magnetic field, respectively. In all cases, the angular momentum flux balance is dominated by the meridional circulation terms with the Coriolis term bringing angular momentum outward and poleward, and the antisolar differential rotation term bringing angular momentum inward and equatorward, and by the Reynolds stresses associated with the convection, which also carry angular momentum inward and equatorward. When summed, the two components of the meridional circulation are a direct reaction to the Reynolds

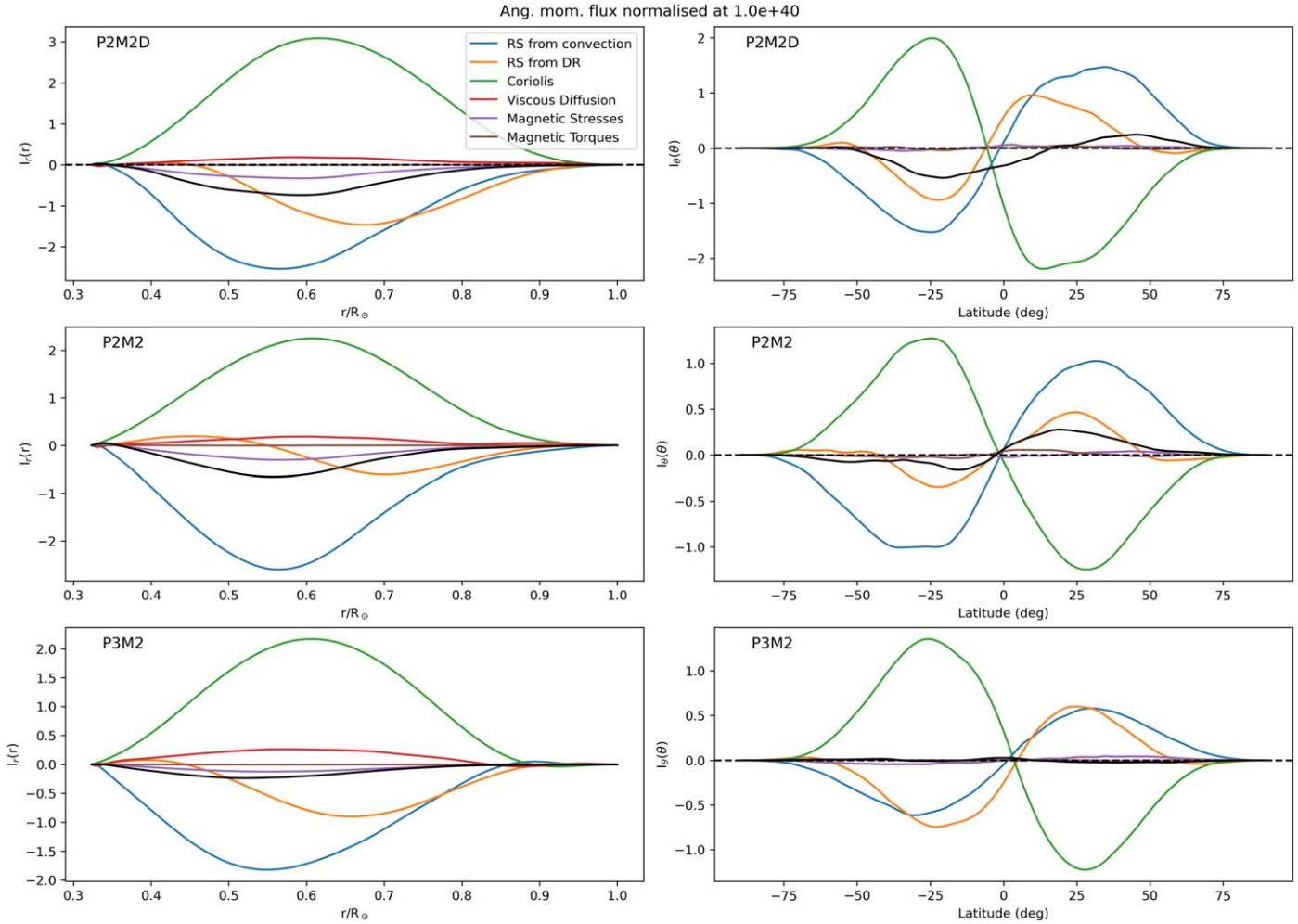

Figure 17. Normalized angular momentum flux balance in radius (left) and latitude (right) for P2M2D (top), P2M2 (middle), and P3M2 (bottom).

stresses, in agreement with the gyroscopic pumping mechanism (M. E. McIntyre 2007).

Appendix C
Evolution of the Velocity and Magnetic Energy Spectra

The starting point in Figure 18 corresponds to the time a magnetic seed is introduced into the simulation. In the left panel of Figure 18 we clearly see that the velocity spectrum barely changes through the simulation. This is indicative that the hydrodynamic regime reached by the simulation is statistically steady. In addition, it displays the very large range of dynamical scales covered by the simulations, with almost three orders of magnitude between the minimum and the maximum in velocity amplitude.

The right panel nicely shows the growth of the magnetic field under the influence of dynamo action. The magnetic field spectrum peaks close to $\ell = 7$ at first, in line with the initial configuration, and then evolves toward smaller scales with $\ell_{\max} = 30$. The growth is continuous for about seven rotation periods, after which time the spectra stack up and do not change, particularly at high ℓ. We therefore expect the dynamics of the magnetic field to be converged after a few rotation periods. We find again a significant amplitude difference between the energy contained at small versus large scales.

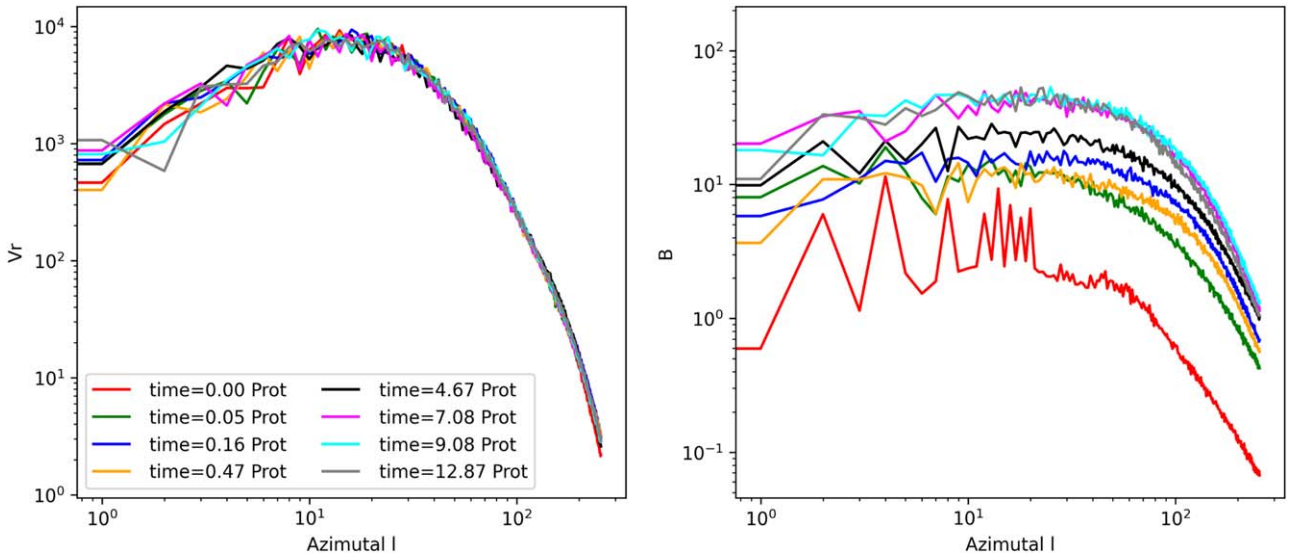

Figure 18. Energy spectra of the velocity (left) and the magnetic field (right) at $R = 0.98R_\star$ of the P3M2 simulation at eight selected times, from the start to the end of the simulation.

ORCID iDs

Louis Amard https://orcid.org/0000-0003-2508-6093
Allan Sacha Brun https://orcid.org/0000-0002-1729-8267

References

Amard, L., Palacios, A., Charbonnel, C., et al. 2019, A&A, 631, A77
Aurière, M., Konstantinova-Antova, R., Charbonnel, C., et al. 2015, A&A, 574, A90
Aurière, M., Konstantinova-Antova, R., Espagnet, O., et al. 2014, in IAU Symp. 302, Magnetic Fields throughout Stellar Evolution, ed. P. Petit, M. Jardine, & H. C. Spruit (Cambridge: Cambridge Univ. Press), 359
Aurière, M., Konstantinova-Antova, R., Petit, P., et al. 2011, A&A, 534, A139
Aurière, M., Petit, P., Mathias, P., et al. 2021, A&A, 646, A130
Aurière, M., Wade, G. A., Konstantinova-Antova, R., et al. 2009, A&A, 504, 231
Bessolaz, N., & Brun, A. S. 2011, AN, 332, 1045
Blouin, S., Mao, H., Herwig, F., et al. 2023, MNRAS, 522, 1706
Browning, M. K., Miesch, M. S., Brun, A. S., & Toomre, J. 2006, ApJL, 648, L157
Brun, A. S., & Browning, M. K. 2017, SoPh, 14, 4
Brun, A. S., Miesch, M. S., & Toomre, J. 2004, ApJ, 614, 1073
Brun, A. S., & Palacios, A. 2009, ApJ, 702, 1078
Brun, A. S., Strugarek, A., Noraz, Q., et al. 2022, ApJ, 926, 21
Brun, A. S., Strugarek, A., Varela, J., et al. 2017, ApJ, 836, 192
Brun, A. S., & Toomre, J. 2002, ApJ, 570, 865
Charbonneau, P. 2005, LRSP, 2, 2
Charbonnel, C., Decressin, T., Lagarde, N., et al. 2017, A&A, 605, A102
Chiavassa, A., Kravchenko, K., & Goldberg, J. A. 2024, LRCA, 10, 2
Clune, T., Elliott, J.-R., Miesch, M.-S., Toomre, J., & Glatzmaier, G. 1999, ParC, 25, 361
Deheuvels, S., Li, G., Ballot, J., & Lignières, F. 2023, A&A, 670, L16
DeRosa, M. L., Brun, A. S., & Hoeksema, J. T. 2012, ApJ, 757, 96
Dorch, S. B. F. 2004, A&A, 423, 1101
Gastine, T., Yadav, R. K., Morin, J., Reiners, A., & Wicht, J. 2014, MNRAS, 438, L76
Gomes, P., & Lopes, I. 2020, MNRAS, 496, 620
Gough, D. O. 1990, in Proc. of the Oji International Seminar, 367, Progress of Seismology of the Sun and Stars, ed. Y. Osaki & H. Shibahashi (Berlin: Springer), 283
Gray, D. F. 2014, ApJ, 796, 88
Hatzes, A. P., & Cochran, W. D. 1993, ApJ, 413, 339
Hatzes, A. P., Cochran, W. D., Endl, M., et al. 2006, A&A, 457, 335
Hatzes, A. P., Zechmeister, M., Matthews, J., et al. 2012, A&A, 543, A98
Jones, C. A., Kuzanyan, K. M., & Mitchell, R. H. 2009, JFM, 634, 291
Käpylä, P. J. 2021, A&A, 655, A78
Käpylä, P. J., Browning, M. K., Brun, A. S., Guerrero, G., & Warnecke, J. 2023, SSRv, 219, 58
Konstantinova-Antova, R., Georgiev, S., Lèbre, A., et al. 2024, A&A, 681, A36
Korhonen, H. 2014, in IAU Symp. 302, Magnetic Fields throughout Stellar Evolution, ed. P. Petit, M. Jardine, & H. C. Spruit (Cambridge: Cambridge Univ. Press), 350
Li, G., Deheuvels, S., Ballot, J., & Lignières, F. 2022, Natur, 610, 43
Li, G., Deheuvels, S., Li, T., Ballot, J., & Lignières, F. 2023, A&A, 680, A26
Lignières, F., Petit, P., Aurière, M., Wade, G. A., & Böhm, T. 2014, in IAU Symp. 302, Magnetic Fields throughout Stellar Evolution, ed. P. Petit, M. Jardine, & H. C. Spruit (Cambridge: Cambridge Univ. Press), 338
Loi, S. T. 2021, MNRAS, 504, 3711
Marsden, S. C., Petit, P., Jeffers, S. V., et al. 2014, MNRAS, 444, 3517
Mathis, S., & Bugnet, L. 2023, A&A, 676, L9
Matt, S. P., Do Cao, O., Brown, B. P., & Brun, A. S. 2011, AN, 332, 897
McFadden, P. L., Merrill, R. T., McElhinny, M. W., & Lee, S. 1991, JGR, 96, 3923
McIntyre, M. E. 2007, in The Solar Tachocline, ed. D. W. Hughes, R. Rosner, & N. O. Weiss (Cambridge: Cambridge Univ. Press), 183
Miesch, M. S., Brun, A. S., & Toomre, J. 2006, ApJ, 641, 618
Miesch, M. S., Elliott, J. R., Toomre, J., et al. 2000, ApJ, 532, 593
Palacios, A., & Brun, A. S. 2007, AN, 328, 1114
Palacios, A., & Brun, A. S. 2014, in IAU Symp. 302, Magnetic Fields throughout Stellar Evolution, ed. P. Petit, M. Jardine, & H. C. Spruit (Cambridge: Cambridge Univ. Press), 363
Palacios, A., Charbonnel, C., Talon, S., & Siess, L. 2006, A&A, 453, 261
Porter, D. H., Woodward, P. R., & Jacobs, M. L. 2000, NYASA, 898, 1
Strassmeier, K. G., Fekel, F. C., Bopp, B. W., Dempsey, R. C., & Henry, G. W. 1990, ApJS, 72, 191
Strugarek, A., Brun, A. S., Mathis, S., & Sarazin, Y. 2013, ApJ, 764, 189
Strugarek, A., Brun, A. S., & Zahn, J. P. 2011, A&A, 532, A34
Takehiro, S.-i., Brun, A. S., & Yamada, M. 2020, ApJ, 893, 83
Tobias, S. M., & Cattaneo, F. 2008, PhRvL, 101, 125003
Woodward, P. R., Porter, D. H., & Jacobs, M. 2003, in ASP Conf. Ser. 293, 3D Stellar Evolution, 293, ed. S. Turcotte, S. C. Keller, & R. M. Cavallo (San Francisco, CA: ASP), 45